Title
Using bidirectional chemical exchange for improved hyperpolarized [13C]bicarbonate pH imaging

Authors
Korenchan, David E
Gordon, Jeremy W
Subramaniam, Sukumar
et al.

Utilizing Bidirectional Chemical Exchange for Improved Hyperpolarized [¹³C]bicarbonate pH Imaging

David E. Korenchan[1,†], **Jeremy W. Gordon**[1], **Sukumar Subramaniam**[1], **Renuka Sriram**[1], **Celine Baligand**[3], **Mark VanCriekinge**[1], **Robert Bok**[1], **Daniel B. Vigneron**[1,2], **David M. Wilson**[1], **Peder E. Z. Larson**[1,2], **John Kurhanewicz**[#1,2], and **Robert R. Flavell**[#1]

[1]Department of Radiology and Biomedical Imaging, University of California—San Francisco, San Francisco, California

[2]UC Berkeley-UCSF Graduate Program in Bioengineering, University of California, San Francisco and University of California, Berkeley, California

[3]Molecular Imaging Research Center, French Alternative Energies and Atomic Energy Commission—Fontenay-aux-Roses, France

[#] These authors contributed equally to this work.

Abstract

Purpose—Rapid chemical exchange can affect signal-to-noise ratio and pH measurement accuracy for hyperpolarized pH imaging with [¹³C]bicarbonate. Therefore, the purpose of this work was to investigate chemical exchange effects on hyperpolarized imaging sequences in order to identify optimal sequence parameters for high signal-to-noise ratio and pH accuracy.

Methods—Simulations were performed under varying rates of bicarbonate-CO_2 chemical exchange to analyze exchange effects on pH quantification accuracy and signal-to-noise ratio under different sampling schemes. Four pulse sequences, including one new technique, a multiple-excitation 2D EPI (multi-EPI) sequence, were compared in phantoms using hyperpolarized [¹³C]bicarbonate, varying parameters such as tip angles, repetition time, order of metabolite excitation, and refocusing pulse design. In vivo hyperpolarized bicarbonate-CO_2 exchange measurements were made in transgenic murine prostate tumors to select in vivo imaging parameters.

Results—Modeling of bicarbonate-CO_2 exchange identified a multiple-excitation scheme for increasing CO_2 signal-to-noise ratio by up to a factor of 2.7. When implemented in phantom imaging experiments, these sampling schemes were confirmed to yield high pH accuracy and signal-to-noise gains. Based on measured bicarbonate-CO_2 exchange in vivo, a 47% CO_2 signal-to-noise gain is predicted.

Conclusion—The novel multi-EPI pulse sequence can boost CO_2 imaging signal in hyperpolarized ¹³C bicarbonate imaging while introducing minimal pH bias, helping to surmount a major hurdle in hyperpolarized pH imaging.

†Correspondence to: Dr. Robert Flavell, Department of Radiology & Biomedical Imaging, UCSF, 185 Berry Street, Lobby 6 Suite 350, Box 0946, San Francisco, CA, 94143, 415-353-3638, Robert.Flavell@ucsf.edu.

Keywords

hyperpolarized ^{13}C; pH imaging; bicarbonate; chemical exchange; MRI; NMR spectroscopy

INTRODUCTION

Dissolution dynamic nuclear polarization, which can provide ^{13}C MR signal gains greater than 10^4 (1), has found primary applications in measuring rapid biological processes, such as lactate dehydrogenase-catalyzed lactate conversion and tissue perfusion in tumors (2). The technology is limited to studying timescales on the order of tens of seconds to a few minutes primarily because most ^{13}C nuclei have T_1 relaxation time constants of a similar magnitude (3). In addition, hyperpolarized (HP) magnetization is non-renewable and must be sampled effectively in order to be useful not only for dynamic NMR spectroscopy, but for MRI as well. Because of these constraints, pulse sequences for HP imaging are designed to be rapid, efficient concerning HP magnetization sampling, and robust to a multitude of factors, including off-resonance effects, susceptibility differences, flow of HP spins in/out of the imaging field of view, pulse power and gradient trajectory miscalibration, and B_0/B_1 inhomogeneity. Because these effects may cause significant errors in quantification of biological parameters, characterization of pulse sequences via simulation and/or imaging phantoms can help identify pulse sequence parameters that mitigate error propagation while optimizing other aspects such as image resolution.

In addition to measuring dynamic metabolic processes, HP MR imaging can also be utilized to image pH, which can affect cellular growth, motility, and function in a wide variety of biological contexts. The mainstay molecule for HP pH imaging is HP [^{13}C]bicarbonate (BiC), which calculates pH on a per-voxel basis by measuring the signal ratio between BiC and CO_2 using a modified Henderson-Hasselbalch equation (4). Although some studies have measured intracellular pH in the heart using [^{13}C]bicarbonate and [13]CO_2 liberated from [1-^{13}C]pyruvate decarboxylation (5–7), most studies have injected HP BiC itself in order to image interstitial pH in tumors (4,8,9), perfused lungs (10,11), and other tissues (12,13). However, HP BiC has several limitations for pH imaging, including low apparent in vivo T_1 (4,8,9) and its sensitivity to field strength and local chemical environment (13,14). In order to address these limitations, we and others have sought to enhance signal through the polarization of bicarbonate precursor molecules (9,10,15), or to use alternative HP ^{13}C imaging agents, including ACES (16), DEMA (17), zymonic acid (18,19), and amino acid derivatives (20). However, BiC remains uniquely appealing for clinical translation, primarily because bicarbonate is routinely administered in a clinical setting.

HP [^{13}C]bicarbonate and [^{13}C]CO_2 present unique challenges to HP imaging. First, the CO_2 magnetization pool is an order of magnitude lower than the bicarbonate pool near physiological pH, due to the low acid dissociation constant ($pK_a = 6.17$) of the bicarbonate-CO_2 buffer system in vivo (4). Second, although bicarbonate and CO_2 manifest as distinct resonances in NMR spectra, they undergo rapid inter-conversion in vitro and in vivo. This serves as a means of magnetization transfer between bicarbonate and CO_2 pools, which can potentially affect imaging signal-to-noise ratio (SNR) and pH quantification via HP imaging.

These effects have not been comprehensively described in the literature, particularly with regard to informing on the choice of pulse sequence design parameters. The goals of this work, therefore, were twofold: first, to characterize the effects that bidirectional bicarbonate-CO_2 chemical exchange has on imaging resolution, SNR, and pH quantification; and second, to identify new strategies for improving CO_2 imaging SNR by exploiting magnetization exchange between metabolites.

METHODS

Measurement of Carbonic Anhydrase-Catalyzed Chemical Exchange In vitro and In vivo

Sodium [^{13}C]bicarbonate (~20 mM) was added to 100 mM phosphate buffer at pH 6.4, along with 7.55 μg/mL of CAII. ^{13}C NMR spectroscopy was performed at 37 °C using a temperature-regulated 500 MHz (^{13}C 125 MHz) Varian INOVA spectrometer (Agilent Technologies, Palo Alto, CA) equipped with a 5 mm triple-tuned, ^{13}C direct-detect, triple-axis gradient-equipped broadband probe (Agilent Technologies, Palo Alto, CA). The bicarbonate-CO_2 chemical exchange was measured with a selective inversion pulse sequence (21). Briefly, a selective 180° inversion pulse (6 ms duration, 500 Hz bandwidth) designed using the Shinnar-Le Roux (SLR) algorithm was applied to the CO_2 resonance, and after an incremented exchange delay a 90° hard pulse-acquire was performed (50 s relaxation delay, 2 s acquisition time, 4 averages/exchange delay, exchange delay incremented from 0.03 to 0.6 s). The 360° hard pulse width was calibrated prior to running the sequence and used to calibrate all other pulses used. Using VnmrJ 4.2A software (Agilent Technologies, Palo Alto, CA), spectra were apodized with a 2 Hz Lorentzian filter, and peak integrals were calculated. The difference between the bicarbonate and CO_2 integrals at each delay were fitted to an exponential of the form $y = a*exp(-bt) + c$, with the decay constant approximating the overall first-order exchange rate $k_{ex} = k_{bc} + k_{cb}$ (21), neglecting T_1 decay ($R_1 \approx 0.03$ s^{-1} at 11.7 T (9)). Additionally, a hard 90° pulse-acquire ^{13}C spectrum was obtained in order to measure the concentration ratio of bicarbonate to CO_2. This ratio was used to calculate the solution pH via the Henderson-Hasselbalch equation as well as to calculate k_{bc} and k_{cb} from k_{ex}, using the equilibrium rate relation $[BiC]k_{bc} = [CO_2]k_{cb}$.

All animal studies were conducted in accordance with the policies of the Institutional Animal Care and Use Committee (IACUC) at the University of California, San Francisco. All in vivo experiments were performed on a vertical-bore 14 T Varian NMR imaging system (150 MHz ^{13}C, Varian Instruments) equipped with a dual-tuned ^{1}H/^{13}C quadrature coil (m2m Imaging, Cleveland, OH). A transgenic adenocarcinoma of the mouse prostate (TRAMP) model mouse supplied by Roswell Park Cancer Institute (Buffalo, NY, USA) was anesthetized with 1-2% isoflurane/100% oxygen at a rate of 1 L/min and cannulated in the lateral tail vein. The anesthetized mouse was secured in an MR-compatible holder with a 37 °C water pad and placed within the vertical bore of the imaging system. Anesthesia was delivered to the mouse via a nose cone, and the breathing rate was monitored using a pressure-sensitive pad located under the spine within the holder. Every 10-12 minutes, the catheter was flushed with 8 μg/mL heparin in normal saline to prevent clotting. ^{1}H anatomical reference images were acquired using a spin echo sequence (0.16 mm in-plane resolution, 40 mm field-of-view, TE/TR = 20/1200 ms). Following HP and dissolution as in

the phantom experiments, 450-500 μL of HP [^{13}C]bicarbonate solution were injected over 12 s, and slice-selective ^{13}C NMR dynamic spectroscopy (10 mm slice placed on tumor, 20° tip, 8 timepoints with 2 s temporal resolution) was initiated 12-13 s after the start of injection. Each spectral acquisition was preceded by 25 spectral suppression sinc pulses (8 ms pulse length) with crusher gradients. The suppression pulse offset for the first four timepoints was set in the middle between bicarbonate and CO_2 and was set to the CO_2 offset for the last four timepoints in order to selectively saturate the CO_2 resonance. Magnitude integrals of the bicarbonate and CO_2 NMR peaks were calculated in VnmrJ, and the first five and last five timepoints were fit to exponential decay curves of the form $y = a*exp(-bt)$ to determine decay rate constants. The bicarbonate->CO_2 first-order rate constant k_{bc} was calculated as the difference in rate constants, as previously described (4). The reverse rate constant k_{cb} and overall rate constant k_{ex} were then calculated using the equations described above for the in vitro kinetics measurements, using the average spectral pH calculated from the first four timepoints.

Chemical Exchange Simulation

All MATLAB code used for simulation is available through GitHub (https://doi.org/10.5281/zenodo.2566620, stored under simulations/bicarbonate-pH_simulation). Bicarbonate-CO_2 chemical exchange effects on imaging resolution and pH accuracy were simulated using the Shinnar-Le Roux algorithm (22) with the "rf_tools" RF pulse design library coupled with the Bloch-McConnell equations implemented in custom MATLAB scripts (MathWorks, Natick, MA). Both Gaussian (256 points, 5-sigma) and sinc (256 points, time-bandwidth = 2) pulse shapes were simulated for the 2D CSI and 2D multi-EPI sequences (described below), respectively. After the first excitation, the xy- and z-magnetization profiles for bicarbonate and CO_2 were scaled based upon the specified pH, denoted as pH_{true}. In between excitations, chemical exchange was simulated between bicarbonate and CO_2 z-magnetization profiles using Bloch-McConnell for a given overall first-order exchange rate k_{ex} and repetition time TR (10 ms spacing between timepoints), neglecting lateral diffusion of spins and T_1 decay. The total signal after each RF pulse was determined by integration along the slice direction. To investigate spatial point-spread function (PSF) broadening over 64 excitations, such as in a 2D CSI [2.78°,25°] BiC/CO_2 excitation scheme, the signal values obtained for each metabolite were arranged in a 2D matrix following a center-out spiral-encoding scheme, and the 2D Fourier transform of this matrix gave the simulated spatial point-spread function. To determine pH accuracy, the acquired bicarbonate and CO_2 signals were summed over all excitations, corrected by the applied tip angles, and used to calculate the measured pH value with the Henderson-Hasselbalch equation, using a pK_a value of 6.17 at 37 °C (4):

$$pH_{meas} = pK_a + \log_{10}\left(\frac{S_{BiC}}{S_{CO_2}} * \frac{\sin\alpha_{CO_2}}{\sin\alpha_{BiC}}\right)$$

The pH error as a function of true pH and tip angle was reported as pH_{meas} - pH_{true}, such that a positive error indicated pH overestimation, and a negative error indicated underestimation.

Bloch-McConnell simulations were also used to study imaging signal-to-noise ratio (SNR) as a function of tip angles, TR, and number of excitations. These simulations did not include the Shinnar-Le Roux algorithm but did include T_1 decay in the Bloch-McConnell equations. Exchange over each TR was simulated using a spacing of 10 ms between timepoints. This timepoint spacing was over 20 times smaller than $1/k_{ex}$, thus sufficiently capturing exchange. T_1 values were assumed to be equal for both metabolites (4,8). The pH_{meas} for a given pH_{true} and set of imaging parameters was calculated as described above. Noise standard deviation was assumed to scale as the square root of the number of excitations.

Phantom Imaging

All phantom imaging utilized the same scanner and coil as the in vivo experiments. A total mass of 54-70 mg of [1-^{13}C]1,2-glycerol carbonate (GLC) was polarized, dissolved, and hydrolyzed as described previously (9), using 2 equivalents of NaOH for hydrolysis. The HP solution was added to each of three 10-mm NMR tubes filled with 100 mM phosphate buffer at three different pH values between 6.0 and 7.8 and kept previously at 37 °C. The final (BiC + CO_2) concentration was 12-35 mM. Just before the dissolution, 7.55 µg/mL of carbonic anhydrase II (CAII, Sigma, St. Louis, MO) were added to each tube. The tubes were injected with HP dissolution, briefly vortexed to mix and inserted into the pre-tuned, pre-shimmed imaging system, which was kept at 37 °C using heated air. The temperature inside the system was calibrated prior via ^{1}H spectroscopy on ethylene glycol (23). The ^{13}C transmitter frequency was calculated from the measured ^{1}H offset of the water resonance. The transfer time between the polarizer and the magnet was 50-80 seconds. The imaging sequence was preceded by a 2° slice-selective pulse-acquire spectrum for SNR normalization between images. After HP ^{13}C imaging with one of four pulse sequences (see next paragraph), a ^{1}H spin-echo axial image was taken for co-registration with the ^{13}C data, and the pH of each tube in the phantom was measured at 37 °C outside the magnet using a conventional pH electrode (Ion 500 series, Oakton Instruments, Vernon Hills, IL) to compare with the pH measured via imaging.

Table 1 summarizes the pulse sequence parameters used for phantom imaging. Other sequence-specific parameters are as follows. For the 2D CSI sequence, phase encoding was performed starting in the center of k-space and spiraling outward. Refocusing in the 3D GRASE sequence was performed either with a 1-band 180° SLR pulse (6 ms length, 500 Hz bandwidth) or a 2-band 180° SLR pulse, with the bands centered on the bicarbonate and CO_2 resonances (2.5 ms length, each band 1200 Hz bandwidth). The pulse sequences tested included one new imaging approach, a multiple-excitation 2D EPI (2D multi-EPI) sequence. This utilized the same sequence as the 2D EPI but acquired multiple timepoints that were summed together in the analysis. The multi-EPI sequence utilized tip angles and TR as determined from simulation to maximize CO_2 SNR enhancements at high pH, and the sequence incorporated slice profile gradient correction over successive excitations (24) by scaling the slice-select gradient by the xy-profile FWHM normalized to the first excitation, as determined via simulation with a constant gradient (see previous section for simulation details). All excitation and refocusing pulses were designed using free MATLAB software developed through the Radiological Sciences Laboratory at Stanford University (available at http://rsl.stanford.edu/research/software.html) (22,25,26). The tip angle correction ratio for

pH calculation corresponding with each excitation scheme was determined using a $[^{13}C]$urea phantom with the same dual-tuned coil and fell within 10% of the theoretical value except when comparing 10° and 90° tip angles with the spectral-spatial pulse (20%); this is likely due to pulse imperfections with a 90° tip.

Data Processing

2D CSI data were analyzed using SIVIC open-source software (Sourceforge.net) (27); all other imaging data were processed using custom MATLAB scripts. For pH calculation, the acquired 2D CSI free induction decays were 10 Hz apodized in the spectral domain, and bicarbonate and CO_2 peak integrals were measured using the magnitude spectra from one voxel within each tube. The phantom 2D EPI and 3D GRASE k-space data were Gaussian-filtered with 12-dB attenuation at the edges. For all pulse sequences, a pH map was calculated on a voxel-by-voxel basis, correcting if necessary for the difference in tip angles on each resonance. A region of interest (ROI) was then drawn for each tube on the pH map, and the average voxel pH was calculated. Voxels with a signal-to-noise ratio (SNR) < 3 were excluded from analysis. SNR comparisons between imaging sequences were performed by zero-filling to 256 in the readout dimension, then reporting the maximum CO_2 peak height/ signal magnitude per tube ROI. The three maxima were then summed, divided by the phased noise standard deviation, and normalized by voxel size, accounting for in-plane and slice profile broadening as determined via simulation, and CO_2 SNR in the 2° slice-selective spectrum acquired just prior to imaging. No spectral or spatial k-space filtering was applied when comparing imaging SNR.

RESULTS

Measurement of Carbonic Anhydrase-Catalyzed Chemical Exchange In vitro and In vivo

The bicarbonate-CO_2 exchange rate under the CAII-catalyzed conditions used in the phantom imaging experiments was measured via CO_2 peak inversion (21). These results are displayed in Figure 1. The pH of solution was measured to be 6.66 via ^{13}C spectroscopy, and the exchange rate constant $k_{ex} = k_{bc} + k_{cb}$ was determined to be 5.51 s^{-1}. Based upon the measured pH and taking the pK$_a$ to equal 6.17 at 37 °C (4), this corresponded to a k_{bc} of 1.34 s^{-1} and a k_{cb} of 4.17 s^{-1}. Assuming these exchange rates to be dominated by the carbonic anhydrase activity and ignoring changes in carbonic anhydrase activity with pH (28), the value of k_{bc} adjusted for pH 7.4 was 0.245 s^{-1}, which is in very good agreement with the value of 0.25 s^{-1} previously measured at similar carbonic anhydrase concentration and pH 7.4 (29).

In order to determine imaging parameters relevant to pH imaging in vivo, we measured HP BiC-CO_2 exchange kinetics in the transgenic adenocarcinoma of the mouse prostate (TRAMP) animal model using selective CO_2 saturation, as previously described (4,29). The inversion technique used in Figure 1 was not feasible for in vivo measurement due to low HP CO_2 signal and inflow/outflow of CO_2 spins. Figure 2 displays images and dynamic slab-selective spectra from a representative mouse. We measured an average tumor pH of 7.16 ± 0.14 and an overall first-order rate constant of 1.56 ± 0.04 s^{-1} (n = 3 mice). This exchange

rate is comparable to similar measurements done using HP [^{13}C]bicarbonate in mouse tumor xenografts (29).

Chemical Exchange Simulation

We utilized Bloch-McConnell simulation in order to model the effects of multiple bicarbonate/CO_2 excitations on spatial resolution and pH. Figures 3a–b display spatial broadening both in-plane (Figure 3a) and in the slice profile (Figure 3b) over a physiological range (6.4-7.6) and under experimental 2D CSI phantom acquisition and chemical exchange conditions ([2.78°,25°] BiC-CO_2 acquisition scheme, Gaussian pulse shape, 64 excitations, $TR = 67$ ms, $k_{ex} = 5.51$ s^{-1}). The spatial point-spread function (PSF) broadening of bicarbonate and CO_2 were approximately equal at each pH value, due to rapid exchange. The broadening was 8% and 1% at pH values of 6.4 and 7.6, respectively (Figure 3a). Slice profile broadening was much more dramatic at low pH, resulting in full-width half-maximum (FWHM) increases of 38% and 42% for bicarbonate and CO_2, respectively, at pH 6.4 (Figure 3b). Although the tip angle on CO_2 was 9-fold higher than on bicarbonate, this led to a modest pH bias of about 0.05 unit across all simulated pH values (Figure 3c).

Single-shot imaging sequences can mitigate these spatial broadening effects, but they can also affect pH accuracy, particularly for faster exchange. Figure 3d summarizes the effects of single-shot sequential excitation tip angle and metabolite order on pH accuracy. Regardless of exchange rate, the error remains below 0.1 pH unit at physiological pH values for $a_{BiC} < 35°$ when bicarbonate is excited first and for $a_{CO2} < 65°$ when CO_2 is excited first.

One distinct advantage of multiple-excitation imaging under bidirectional exchange is that it can induce z-magnetization shuttling from bicarbonate to CO_2 if unequal tip angles are used on each metabolite. This is illustrated by Bloch-McConnell simulation under 2D CSI [2.78°, 25°] BiC/CO_2 acquisition conditions in Figure 4a. Compared with the no-exchange case, chemical exchange under a [2.78°,25°] BiC-CO_2 acquisition scheme leads to a 2.2- to 4.2-fold CO_2 signal enhancement depending on pH, with greater enhancement occurring for higher pH values. We were therefore motivated to simulate exchange-mediated CO_2 SNR enhancement while varying multiple acquisition parameters, including BiC and CO_2 tip angles, TR, and number of excitations N_{exc} (Figure 4b). The simulation revealed an acquisition scheme $[a_{BiC}, a_{CO2}, TR] = [5°, 52°, 330ms]$ that would provide a 2.7-fold CO_2 SNR increase over a single 90° excitation at pH 7.6 ($N_{exc} = 43$) and a 1.3-fold increase at pH 6.4 ($N_{exc} = 8$). The associated |pH error| was below 0.05 unit at each pH value. This acquisition scheme was later implemented in the phantom imaging.

Phantom Imaging

Representative maps of hyperpolarized [^{13}C]bicarbonate, [^{13}C]CO_2, and pH are displayed in Figure 5 for the three conventional pulse sequences tested (2D CSI [2.78°,25°], 2D EPI 10° BiC -> 90° CO_2, 3D GRASE 10° BiC -> 90° CO_2 + 2-band refocusing). The acquisition parameters were set based upon what simulation predicted would provide the best pH accuracy while maximizing CO_2 SNR. Even so, the 2D EPI and 3D GRASE sequences generally showed lower CO_2 SNR than the 2D CSI, particularly in the high pH tube. This is

likely because BiC->CO$_2$ z-magnetization shuttling during 2D CSI acquisition increases the imaging SNR while minimally biasing pH (see Figures 3c, 4a).

In order to combine exchange-mediated signal enhancement with the versatility of a single-shot imaging sequence, we performed phantom imaging using a multiple-excitation 2D EPI (multi-EPI) sequence (Figure 6), using acquisition parameters derived from our Bloch-McConnell simulation (see Figure 4b). The mean bicarbonate and CO$_2$ SNR for each pH value varied as a function of summed excitations, with both metabolite SNRs reaching a peak for approximately the same number of excitations at each pH value (Figure 7a). The mean calculated pH from the summed excitation maps remained within ±0.1 pH unit from the true pH, as determined via pH electrode, over all excitations. Additionally, the peak CO$_2$ SNR enhancement at each pH matched closely with the enhancements predicted by simulation; the mean enhancement fell within ±10% of the predicted value at each pH value (Figure 7b). This also translated into an overall CO$_2$ SNR boost of about 38% compared with the 2D CSI [2.78°,25°] BiC/CO$_2$ excitation scheme (Figure 7c).

DISCUSSION

Hyperpolarized pH imaging with [^{13}C]bicarbonate is unique in the field of HP imaging in that its chemical conversion to ^{13}CO$_2$ is both relatively rapid and bidirectional. While the first-order rate constant for conversion of pyruvate to lactate has been measured with HP imaging to be on the order of 0.01-0.07 s^{-1} in mice and humans (30–33), bicarbonate-CO$_2$ exchange kinetics start at 0.15 s^{-1} for the uncatalyzed reaction and are typically accelerated in vivo by the carbonic anhydrase enzyme. Table 2 provides a literature summary of measured rate constants in biological systems relevant to HP pH imaging. Importantly, HP [^{13}C]bicarbonate can itself be used to measure exchange kinetics and carbonic anhydrase activity in vivo, as has been previously reported (4,29). The bidirectional nature of exchange also holds important ramifications with regards to magnetization exchange during HP imaging. [^{13}C]bicarbonate and ^{13}CO$_2$ fall within a slow-exchange NMR regime in vivo, in which the overall exchange rate constant is much lower than the chemical shift separation (in Hz) between the two resonances (ie. k$_{ex}$ << f). This means that each resonance can be individually excited, inverted, and/or refocused, enabling a wide variety of opportunities for manipulating the magnetization pools. However, if the interconversion between the two pools is fast relative to timescales of imaging, then it can affect spatial resolution, signal-to-noise ratio, and pH accuracy depending on pulse sequence design. We therefore set out to not only study these effects but also identify new strategies of boosting SNR and imaging resolution while mitigating pH inaccuracy.

Bloch-McConnell simulation of HP magnetization dynamics reveals several effects of bicarbonate-CO$_2$ sampling on imaging resolution and pH accuracy that we confirmed in phantoms. By utilizing separate tip angles on bicarbonate and CO$_2$, one can perturb the equilibrium between their z-magnetizations, causing net flow of magnetization from one to the other. This same principle applies when one metabolite is selectively inverted, except that magnetization exchange between pools now becomes disruptive. Indeed, this "Le Chatelier's principle" of magnetization exchange forms the basis of NMR techniques for measuring exchange kinetics (4,21,29). In the context of pH imaging, however, strong

coupling of the bicarbonate and CO_2 pools due to rapid exchange (relative to imaging timescales) can produce both negative and positive effects. On the negative side, rapid exchange relative to the imaging timescale can lead to pH inaccuracies for sequential-excitation, single-shot sequences such as 2D EPI and 3D GRASE, especially if the first tip angle is large (Figures 3d, 7b). Additionally, if only one metabolite is selectively inverted over a spin-echo sequence, rapid exchange between odd spin echoes will lead to destructive magnetization exchange and dramatically affect SNR and pH accuracy (see Supporting Information Figure S1c). On the positive side, for multi-excitation 2D slice-selective sequences such as the 2D CSI and 2D multi-EPI, rapid exchange works to equalize in-plane spatial broadening (Figure 3a) and/or slice profile effects (Figure 3b) between bicarbonate and CO_2, as well as mitigate pH measurement errors (Figures 3c, 6a). Most importantly, magnetization shuttling can be exploited by using a higher tip angle on CO_2 in order to boost the CO_2 signal (Figure 4a), which is always lower than bicarbonate over the physiological pH range. This approach has been previously implemented in cardiac pH dynamic imaging (7). The CO_2 signal boost is greater at high pH, where a larger fraction of the HP magnetization resides in the bicarbonate pool. In this way, one can choose magnetization sampling and timing parameters so as to maximize CO_2 SNR over multiple excitations without compromising pH accuracy, given *a priori* knowledge of the timescales of exchange and T_1 relaxation (Figure 4b, Figure 7). Table 3 summarizes these positive and negative effects of rapid BiC-CO_2 exchange for all pulse sequences implemented in this study.

The 2D multi-EPI sequence reported herein offers distinct advantages over conventional 2D CSI, as well as single-shot gradient- and/or spin-echo sequences. Although both 2D CSI [2.78°,25°] and 2D multi-EPI demonstrate significant SNR gains over single-shot sequences due to BiC->CO_2 magnetization shuttling, they differ significantly in acquisition and reconstruction. Proper 2D CSI reconstruction is contingent on obtaining sufficient SNR for all acquired FIDs; if later acquisitions are below the noise floor, then spatial information is effectively lost. Additionally, later excitations can experience slice profile distortion due to oversampling in the middle of the slice (24), particularly for CO_2, as demonstrated in Figure 3b. Thus, one must take care not to sample the total bicarbonate-CO_2 magnetization pool too heavily; however, this in turn limits SNR. In contrast, the multi-EPI offers considerable flexibility with regards to image reconstruction while maintaining high fidelity to the prescribed imaging resolution. In principle, the BiC and CO_2 SNR for a given voxel can be plotted as a function of summed excitations, allowing the user to choose the number of excitations that maximizes the lower SNR of the two and thus provides the highest pH accuracy. However, the true voxel pH accuracy will ultimately depend on the local rate of BiC-CO_2 exchange, which varies between tissues and compartments (see Table 1) and is likely to vary throughout the same tissue. Nevertheless, one can select parameters based upon a minimum expected exchange rate, since faster exchange in the context of multi-EPI leads to higher pH accuracy. The multi-EPI is not immune to slice profile broadening over multiple excitations, particularly at lower pH values where the higher CO_2 tip angle depletes the total HP magnetization pool more rapidly. This broadening was reduced experimentally using gradient correction (24), although simulation still predicted a 17% broadening for the CO_2 slice profile at pH 6.4. In principle, the multi-excitation approach could be extended to

other pulse sequences suitable for dynamic measurement, including 2D echo-planar spectroscopic imaging (EPSI) and 3D imaging. Thus, it offers a great deal of flexibility for pH imaging.

Some practical concerns that apply generally to all pH imaging sequences herein are worth noting. First, pulse power miscalibration, especially when using large tip angles on CO_2, can lead to pH inaccuracy via error in the tip angle correction factor, $\sin(a_{CO2})/\sin(a_{BiC})$. Second, transmit B_1 inhomogeneity can further lead to inaccuracy in pH measurement. To correct for these, pulse calibration and B_1 mapping could be performed on a ^{13}C thermal phantom prior to HP imaging (34), or B_1 mapping could potentially be performed during the HP experiment using a Bloch-Siegert based approach in real time (35). Thirdly, miscalibration of 180° pulse power in spin-echo sequences can lead to signal losses in the second excited resonance via incomplete inversion. This effect is expected to increase with more refocusing pulses. This consideration makes the utilization of spin-echo sequences challenging for rapidly exchanging systems, especially when considering B_1 inhomogeneity throughout the imaging volume. This could potentially be resolved by using adiabatic refocusing pulses (36,37), but this was not a viable alternative for the high-field imaging herein, due to the high pulse bandwidth requirements in order to refocus both metabolites (~5.3 kHz separation at 14 T).

Inherent in all MR-based pH measurement techniques is the assumption that the reporter compound has reached equilibrium at the pH to be measured (38). This means in the context of HP pH imaging that the HP agent must be given sufficient time to equilibrate, with the sum of the forward and backward first-order rate constants, k_{ex}, describing the timescale to equilibration (21). Using the number for k_{ex} in blood from Table 3, for example, gives a characteristic time constant of 680 ms; thus, HP BiC in blood is expected to be 95% equilibrated in three time constants, or ~2 s. Acceleration of BiC-CO_2 exchange by carbonic anhydrase, therefore, also plays an important role in enforcing pH accuracy by quickly equilibrating inflowing HP molecules to the interstitial pH.

The multi-EPI approach described herein holds promise for in vivo translation, as well as eventual clinical implementation. Using the BiC-CO_2 kinetic rate constant determined in TRAMP tumors and assuming an in vivo T_1 of 10 s (4,8), simulation predicts a 47% boost in CO_2 imaging SNR over a single 90° excitation at a tumor pH of 7.2, as was measured in this study. The EPI sequence with spectral-spatial excitation is also readily implemented on a clinical MRI scanner, facilitating eventual clinical translation. One disadvantage with any multi-excitation sequence, however, is the long imaging time during which various in vivo processes could contribute to pH inaccuracy, such as inflow of bicarbonate/CO_2 spins that have not yet reached pH equilibrium or transient changes in voxel pH, such as might be caused by pCO_2 fluctuations (39). Additionally, multiple excitations can result in specific absorption rate (SAR) concerns for patients, especially if used with a spin-echo sequence. Nevertheless, these concerns can likely be managed without serious detriment to the gains in SNR attainable with a multi-excitation approach. One final consideration regarding clinical implementation of pH imaging is that the short BiC/CO_2 T_1 in vivo, measured as ~10 s within various mouse/rat tissues at field strengths ranging from 3-14 T (4,8,9,13), may be prohibitive for future translation into patients. It has been suggested that this may be due to

fast macromolecular binding-unbinding kinetics (13), in which case a short interstitial T_1 would be an insurmountable problem. However, in humans there may be greater preservation of vascular HP BiC/CO_2 signal prior to tissue delivery, owing to a slower cardio-respiratory cycle compared with rodents. This, in turn, would result in less global HP signal loss due to CO_2 exchange and exhalation in the lungs (8,11). Additionally, patients could be asked to perform a breath hold during injection and imaging, further reducing HP signal loss via the lungs. These considerations suggest that clinical translation of HP BiC is feasible, although this can only be validated via HP imaging in larger mammals.

In conclusion, we demonstrated effects of chemical exchange on imaging parameters relevant to in vivo HP imaging. Chemical exchange was found to affect imaging point-spread function and slice profile over the course of multiple excitations, as well as pH accuracy when rapid exchange occurred between excitations and refocusing pulses. Magnetization exchange between bicarbonate and CO_2 was also found to result in CO_2 SNR increases with heavier sampling on the CO_2 pool, and this was demonstrated in a 2D multi-EPI imaging approach. This strategy holds great promise for improving imaging SNR while remaining faithful to the prescribed spatial resolution and reducing pH inaccuracy. Furthermore, the technique will likely lead to imaging SNR gains in vivo, surmounting limitations in HP pH imaging with HP $[^{13}C]$bicarbonate.

Supplementary Material

Refer to Web version on PubMed Central for supplementary material.

ACKNOWLEDGMENTS

REFERENCES

1. Ardenkjaer-Larsen JH, Fridlund B, Gram A, Hansson G, Hansson L, Lerche MH, Servin R, Thaning M, Golman K. Increase in signal-to-noise ratio of > 10,000 times in liquid-state NMR. PNAS 2003;100:10158–10163. [PubMed: 12930897]

2. Sriram R, Kurhanewicz J, Vigneron DB. Hyperpolarized 13C MRI and MRS Studies In: Bottomley PA, Griffiths JR, editors. Handbook of Magnetic Resonance Spectroscopy In Vivo. Chichester, UK; 2016 pp. 659–678.

3. Keshari KR, Wilson DM. Chemistry and biochemistry of 13 C hyperpolarized magnetic resonance using dynamic nuclear polarization. Chem Soc Rev 2014;43:1627–1659. [PubMed: 24363044]

4. Gallagher FA, Kettunen MI, Day SE, et al. Magnetic resonance imaging of pH in vivo using hyperpolarized 13C-labelled bicarbonate. Nature 2008;453:940–943. [PubMed: 18509335]

5. Schroeder MA, Swietach P, Atherton HJ, Gallagher FA, Lee P, Radda GK, Clarke K, Tyler DJ. Measuring intracellular pH in the heart using hyperpolarized carbon dioxide and bicarbonate: a 13C and 31P magnetic resonance spectroscopy study. Cardiovasc Res 2010;86:82–91. doi: 10.1093/cvr/cvp396. [PubMed: 20008827]

6. Lau AZ, Miller JJ, Tyler DJ. Mapping of intracellular pH in the in vivo rodent heart using hyperpolarized [1-13C]pyruvate. Magn Reson Med 2017;77:1810–1817. doi: 10.1002/mrm.26260. [PubMed: 27173806]

7. Chen AP, Hurd RE, Schroeder MA, Lau AZ, Gu Y-P, Lam WW, Barry J, Tropp J, Cunningham CH. Simultaneous investigation of cardiac pyruvate dehydrogenase flux, Krebs cycle metabolism and pH, using hyperpolarized [1,2-13C2]pyruvate in vivo. NMR Biomed. 2011;25:305–311. doi: 10.1002/nbm.1749. [PubMed: 21774012]

8. Wilson DM, Keshari KR, Larson PEZ, et al. Multi-compound polarization by DNP allows simultaneous assessment of multiple enzymatic activities in vivo. J Magn Reson 2010;205:141–147. [PubMed: 20478721]

9. Korenchan DE, Flavell RR, Baligand C, Sriram R, Neumann K, Sukumar S, VanBrocklin H, Vigneron DB, Wilson DM, Kurhanewicz J. Dynamic nuclear polarization of biocompatible 13C-enriched carbonates for *in vivo* pH imaging. Chem Commun 2016;52:3030–3033. doi: 10.1039/C5CC09724J.

10. Ghosh RK, Kadlecek SJ, Pourfathi M, Rizi RR. Efficient production of hyperpolarized bicarbonate by chemical reaction on a DNP precursor to measure pH. Magn Reson Med 2014;74:1406–1413. doi: 10.1002/mrm.25530. [PubMed: 25393101]

11. Drachman N, Kadlecek S, Pourfathi M, Xin Y, Profka H, Rizi R. In vivo pH mapping of injured lungs using hyperpolarized [1– 13C]pyruvate. Magn Reson Med 2016;78:1121–1130. doi: 10.1002/mrm.26473. [PubMed: 27714832]

12. Scholz DJ, Janich MA, Kollisch U, Schulte RF, Ardenkjaer-Larsen JH, Frank A, Haase A, Schwaiger M, Menzel MI. Quantified pH imaging with hyperpolarized 13C-bicarbonate. Magn Reson Med [Internet] 2014;73:2274–2282. doi: 10.1002/mrm.25357.

13. Scholz DJ, Otto AM, Hintermair J, et al. Parameterization of hyperpolarized 13C-bicarbonate-dissolution dynamic nuclear polarization. Magn Reson Mater Phy 2015;28:591–598. doi: 10.1007/s10334-015-0500-9.

14. Martínez-Santiesteban FM, Dang TP, Lim H, Chen AP, Scholl TJ. T1nuclear magnetic relaxation dispersion of hyperpolarized sodium and cesium hydrogencarbonate-13C. NMR Biomed. 2017;30:e3749–8. doi: 10.1002/nbm.3749.

15. Maptue N, Jiang W, Harrison C, Funk AM, Sharma G, Malloy CR, Sherry D, Khemtong C. Esterase-Catalyzed Production of Hyperpolarized 13C-Enriched Carbon Dioxide in Tissues for Measuring pH. ACS Sensors 2018;3:2232–2236. doi: 10.1021/acssensors.8b01097. [PubMed: 30398335]

16. Flavell RR, Morze von C, Blecha JE, et al. Application of Good's buffers to pH imaging using hyperpolarized 13C MRI. Chem Commun 2015;51:14119–14122. doi: 10.1039/C5CC05348J.

17. Korenchan DE, Taglang C, Morze von C, et al. Dicarboxylic acids as pH sensors for hyperpolarized (13)C magnetic resonance spectroscopic imaging. Analyst 2017;142:1429–1433. [PubMed: 28322385]

18. Düwel S, Hundshammer C, Gersch M, et al. Imaging of pH in vivo using hyperpolarized. Nature 2017;8:1–9. doi: 10.1038/ncomms15126.

19. Hundshammer C, Düwel S, Köcher SS, Maltee G, Feuerecker B, Scheurer C, Haase A, Glaser SJ, Schwaiger M, Schilling F. Deuteration of Hyperpolarized 13C-Labeled Zymonic Acid Enables Sensitivity-Enhanced Dynamic MRI of pH. ChemPhysChem 2017;18:2422–2425. doi: 10.1002/cphc.201700779. [PubMed: 28719100]

20. Hundshammer C, Düwel S, Ruseckas D, et al. Hyperpolarized Amino Acid Derivatives as Multivalent Magnetic Resonance pH Sensor Molecules. Sensors 2018;18: doi: 10.3390/s18020600.

21. Dahlquist FW, Longmuir KJ, Vernet Du RB. Direct Observation of Chemical Exchange by a Selective Pulse NMR Technique. J Magn Reson 1975:406–410.

22. Pauly J, Le Roux P, Nishimura D, Macovski A. Parameter relations for the Shinnar-Le Roux selective excitation pulse design algorithm (NMR imaging). IEEE Trans. Med. Imaging 1991;10:53–65. doi: 10.1109/42.75611. [PubMed: 18222800]

23. Raiford DS, Fisk CL, Becker ED. Calibration of Methanol and Ethylene-Glycol Nuclear Magnetic-Resonance Thermometers. Anal Chem 1979;51:2050–2051.

24. Gordon JW, Milshteyn E, Marco-Rius I, Ohliger M, Vigneron DB, Larson PEZ. Mis-estimation and bias of hyperpolarized apparent diffusion coefficient measurements due to slice profile effects. Magn Reson Med 2016;78:1087–1092. [PubMed: 27735082]

25. Larson PEZ, Kerr AB, Chen AP, Lustig MS, Zierhut ML, Hu S, Cunningham CH, Pauly JM, Kurhanewicz J, Vigneron DB. Multiband excitation pulses for hyperpolarized C-13 dynamic chemical-shift imaging. Journal of Magnetic Resonance 2008;194:121–127. doi: 10.1016/j.jmr. 2008.06.010. [PubMed: 18619875]

26. Kerr AB, Larson PE, Lustig M. Multiband spectral-spatial design for high-field and hyperpolarized C-13 applications. In:; 2008.

27. Crane JC, Olson MP, Nelson SJ. SIVIC: Open-Source, Standards-Based Software for DICOM MR Spectroscopy Workflows. International Journal of Biomedical Imaging 2013;2013:1–12. doi: 10.1002/mrm.20663.

28. McIntyre A, Patiar S, Wigfield S, et al. Carbonic Anhydrase IX Promotes Tumor Growth and Necrosis In Vivo and Inhibition Enhances Anti-VEGF Therapy. Clin. Cancer Res. 2012;18:3100–3111. doi: 10.1158/1078-0432.CCR-11-1877. [PubMed: 22498007]

29. Gallagher FA, Sladen H, Kettunen MI, et al. Carbonic Anhydrase Activity Monitored In Vivo by Hyperpolarized 13C-Magnetic Resonance Spectroscopy Demonstrates Its Importance for pH Regulation in Tumors. Cancer Res 2015;75:4109–4118. doi: 10.1158/0008-5472.CAN-15-0857. [PubMed: 26249175]

30. Chen H-Y, Larson PEZ, Bok RA, et al. Assessing Prostate Cancer Aggressiveness with Hyperpolarized Dual-Agent 3D Dynamic Imaging of Metabolism and Perfusion. Cancer Res 2017;77:3207–3216. [PubMed: 28428273]

31. Nelson SJ, Kurhanewicz J, Vigneron DB, et al. Metabolic Imaging of Patients with Prostate Cancer Using Hyperpolarized [1-13C]Pyruvate. Sci Transl Med 2013;5:198ra108–198ra108. doi: 10.1126/scitranslmed.3006070.

32. Aggarwal R, Vigneron DB, Kurhanewicz J. Hyperpolarized 1-[13C]-Pyruvate Magnetic Resonance Imaging Detects an Early Metabolic Response to Androgen Ablation Therapy in Prostate Cancer. Eur Urol 2017;72:1028–1029. [PubMed: 28765011]

33. Chen H-Y, Larson PEZ, Gordon JW, et al. Technique development of 3D dynamic CS-EPSI for hyperpolarized 13C pyruvate MR molecular imaging of human prostate cancer. Magn Reson Med 2018;77:3207–11.

34. Koelsch BL, Reed GD, Keshari KR, Chaumeil MM, Bok R, Ronen SM, Vigneron DB, Kurhanewicz J, Larson PEZ. Rapid in vivo apparent diffusion coefficient mapping of hyperpolarized 13C metabolites. Magn Reson Med 2014;74:622–633. doi: 10.1002/mrm.25422. [PubMed: 25213126]

35. Tang S, Milshteyn E, Reed G, Gordon J, Bok R, Zhu X, Zhu Z, Vigneron DB, Larson PEZ. A regional bolus tracking and real-time B 1calibration method for hyperpolarized 13C MRI. Magn Reson Med 2018;3:37–13.

36. Bernstein MA, King KF, Zhou XJ. Handbook of MRI pulse sequences. Elsevier Academic Press; 2004.

37. Cunningham CH, Chen AP, Albers MJ, Kurhanewicz J, Hurd RE, Yen Y-F, Pauly JM, Nelson SJ, Vigneron DB. Double spin-echo sequence for rapid spectroscopic imaging of hyperpolarized 13C. Journal of Magnetic Resonance 2007;187:357–362. [PubMed: 17562376]

38. Gallagher FA, Kettunen MI, Brindle KM. Imaging pH with hyperpolarized 13C Rizi R, editor. NMR Biomed. 2011;24:1006–1015. doi: 10.1002/nbm.1742. [PubMed: 21812047]

39. Hulikova A, Aveyard N, Harris AL, Vaughan-Jones RD, Swietach P. Intracellular carbonic anhydrase activity sensitizes cancer cell pH signaling to dynamic changes in CO2 partial pressure. J Biol Chem 2014;289:25418–25430. [PubMed: 25059669]

40. Berg JM, Tymoczko JL, Stryer L. Making a Fast Reaction Faster: Carbonic Anhydrases In: Biochemistry. 5 ed New York: W H Freeman; 2002.

41. Geers C, Gros G. Carbon dioxide transport and carbonic anhydrase in blood and muscle. Physiol. Rev 2000;80:681–715. [PubMed: 10747205]

42. Itada N, Forster RE. Carbonic anhydrase activity in intact red blood cells measured with 18O exchange. Journal of Biological Chemistry 1977;252:3881–3890. [PubMed: 405387]

43. Leem CH, Vaughan-Jones RD. Out-of-equilibrium pH transients in the guinea-pig ventricular myocyte. J. Physiol. 1998;509 (Pt 2):471–485. [PubMed: 9575296]
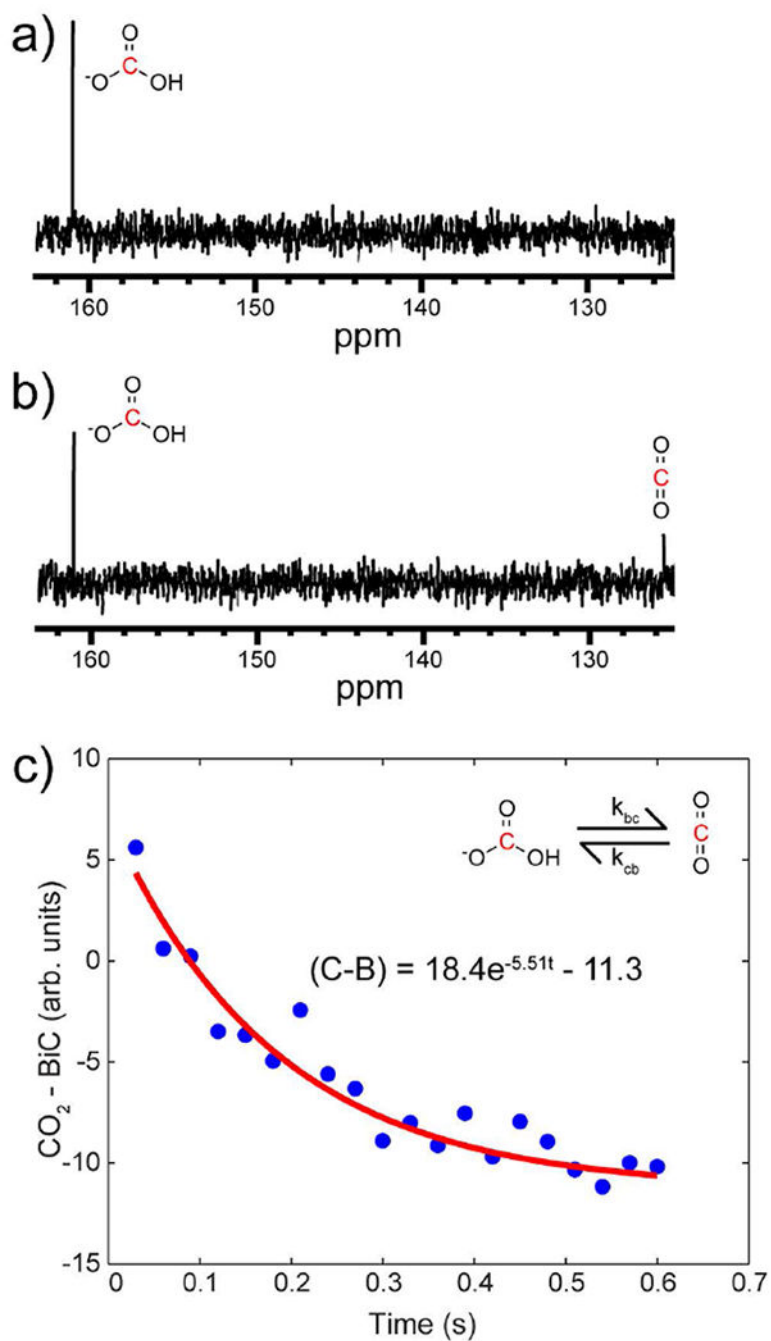
Figure 1:

Measurement of bicarbonate-CO_2 exchange in a thermally polarized phantom via selective CO_2 inversion and ^{13}C NMR dynamic spectroscopy. (a-b) Spectra showing $[^{13}C]$bicarbonate and $^{13}CO_2$ resonances at (a) 0.03 s and (b) 0.54 s after selective CO_2 inversion. (c) Exponential fitting of (bicarbonate - CO_2) signal difference in order to obtain $k_{ex} = k_{bc} + k_{cb}$ = 5.51 s^{-1}. T_1 contribution to decay is negligible ($R_1 \approx 0.03$ s^{-1} at 11.7 T).
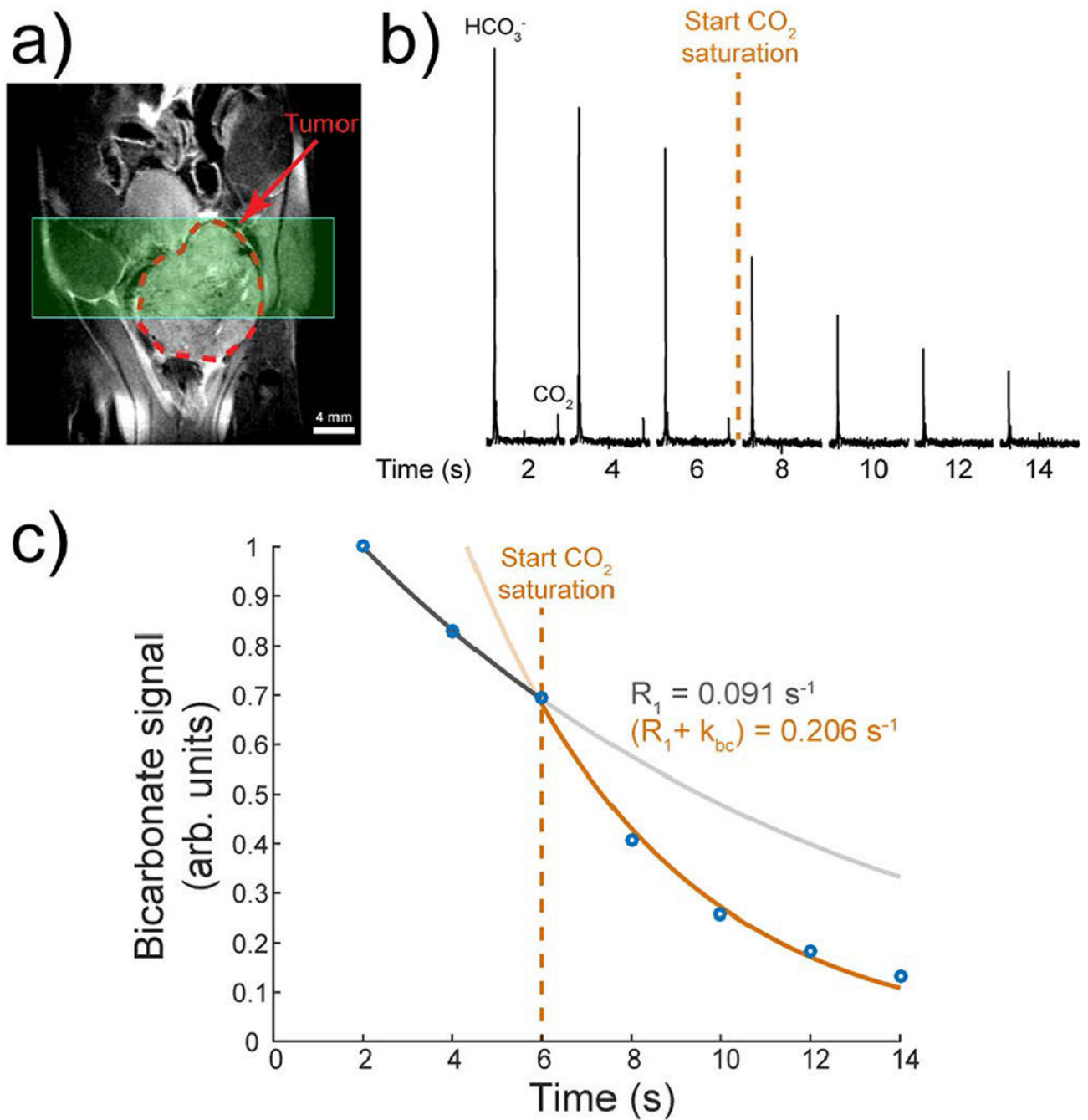
Figure 2:

Measurement of in vivo bicarbonate-CO_2 exchange in transgenic murine prostate cancer. (a) Coronal ^1H image of a representative TRAMP mouse showing tumor and slice placement for dynamic ^{13}C NMR spectroscopy. (b) Slice-selective dynamic ^{13}C NMR spectra showing faster [^{13}C]bicarbonate signal decay with selective $^{13}CO_2$ saturation. Average pH was calculated from spectra to be 7.26. (c) Fitting bicarbonate signal decays before and after selective $^{13}CO_2$ saturation determines both T_1 decay and forward exchange rate constant,

k_{bc}. Using the average spectral pH, the overall exchange rate constant is calculated as $k_{ex} = k_{bc}(1 + 10^{pH-pKa}) = 1.53$ s^{-1}.
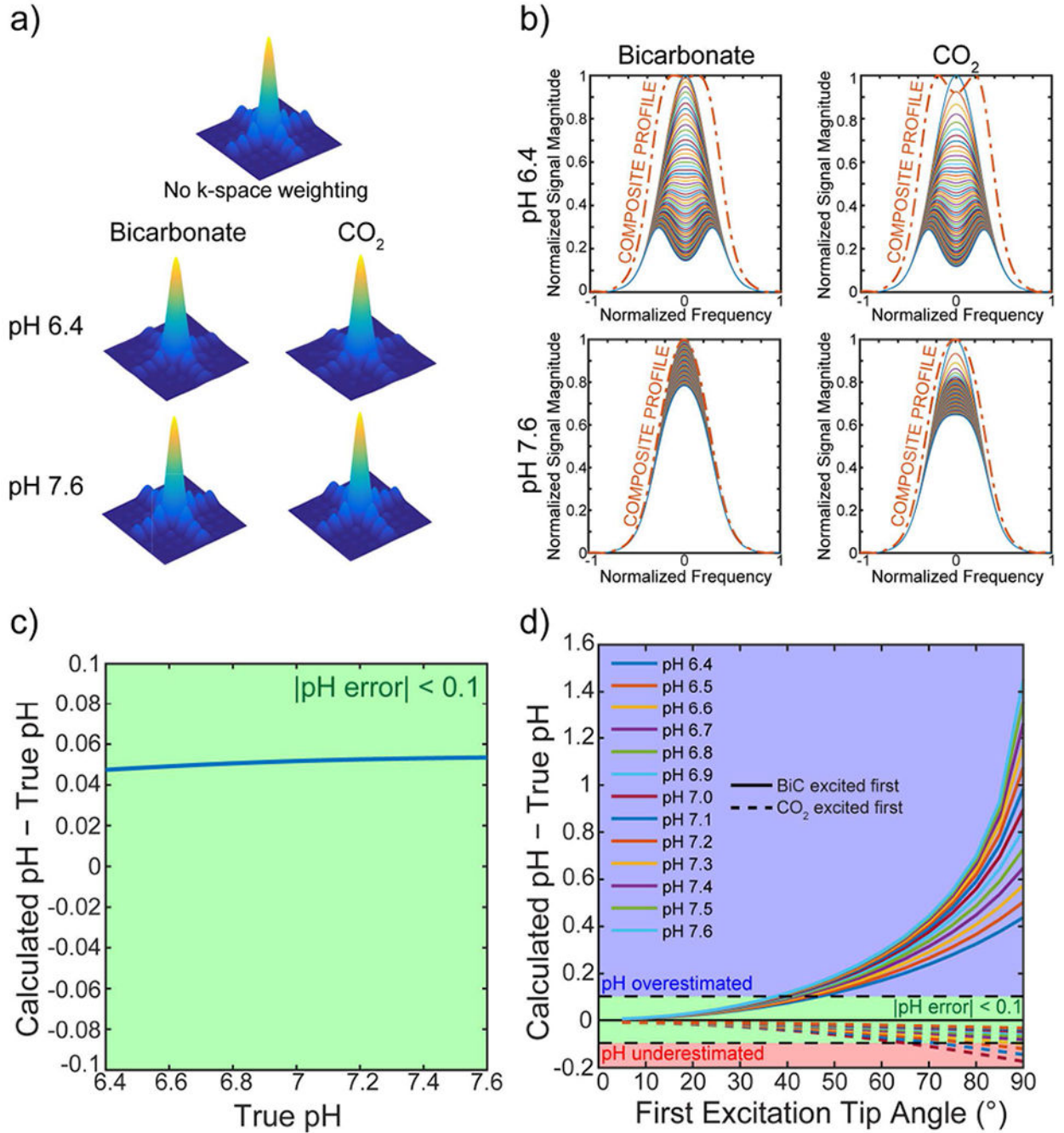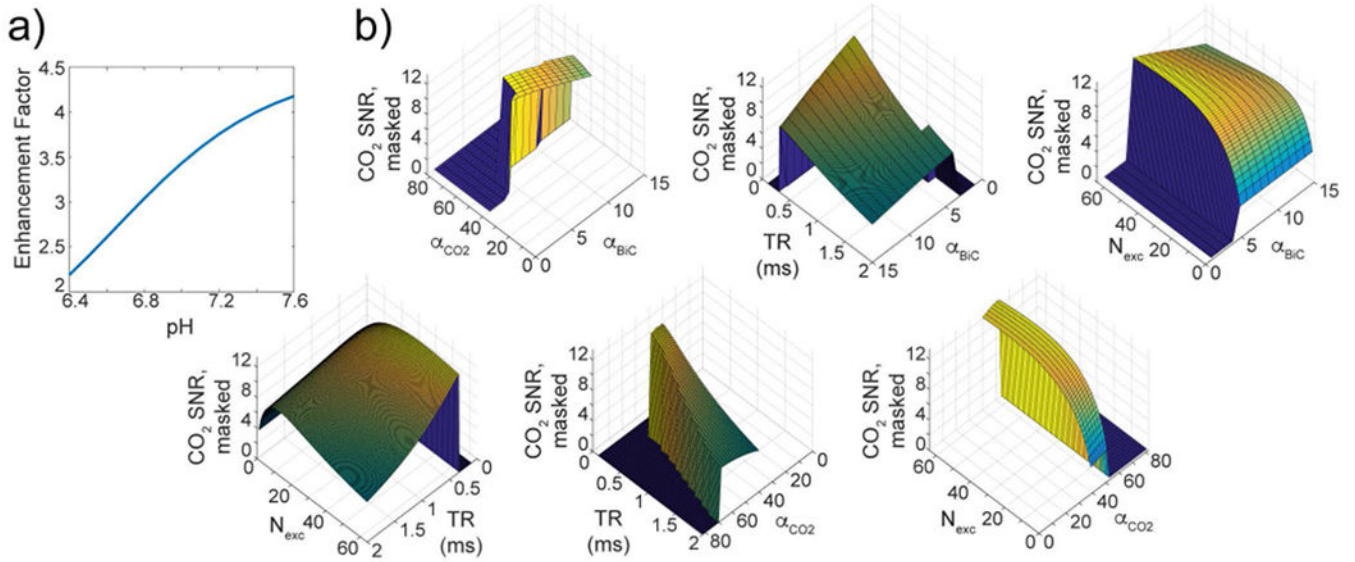
Figure 3:

Simulation results of $[^{13}C]$bicarbonate pH imaging. (a-c) Simulations of spatial resolution and pH accuracy under conditions relevant to the 2D CSI phantom imaging performed (64 excitations, Gaussian pulse, $[2.78°, 25°]$ BiC/CO_2 tip angles, $k_{ex} = 5.51$ s^{-1}, $TR = 67$ ms, T_1 decay neglected). (a) Chemical exchange causes similar in-plane spatial broadening to occur for both bicarbonate and CO_2, but greater broadening is observed at lower pH values due to more signal in the CO_2 pool (8% broadening increase at pH 6.4, 1% increase at pH 7.6). (b) Slice profile effects with chemical exchange. The composite profile of all 64 excitations is

significantly broader at pH 6.4 (38% broadening BiC, 42% broadening CO_2) than at pH 7.6 (1% broadening, both metabolites) (c) pH accuracy remains within 0.06 pH unit even with higher sampling on CO_2. (d) Imaging pH error for a single-shot sequence (e.g. 2D EPI) as a function of first excitation tip angle under complete chemical exchange. pH error is kept below 0.1 pH unit for all pH values if $a_{BiC} < 35°$ or if $a_{CO2} < 65°$.

Figure 4:
Simulation results exploring multi-excitation magnetization shuttling to improve CO_2 SNR.
(a) Enhancement of CO_2 signal-to-noise ratio over no-exchange case ($k_{ex} = 0$), using
simulation parameters listed for Figure 2. Net enhancement ranges from 2.2 to 4.2, with
greater enhancement at pH 7.6. (b) Simulation for phantom conditions of CO_2 signal-to-
noise ratio at pH 7.6 as a function of bicarbonate/CO_2 tip angles, TR, and number of
excitations. For each plot, the unplotted parameters are set to the values that maximize CO_2
SNR. SNR has been set to 0 for parameter combinations that lead to $|pH\ error| > 0.05$ unit
and/or the low-pH BiC SNR being lower than the high-pH CO_2 SNR over simulated pH
range. Simulation parameters: $T_1 = 25$ s (both metabolites), $k_{ex} = 4.32$ s^{-1} (adjusted for pH
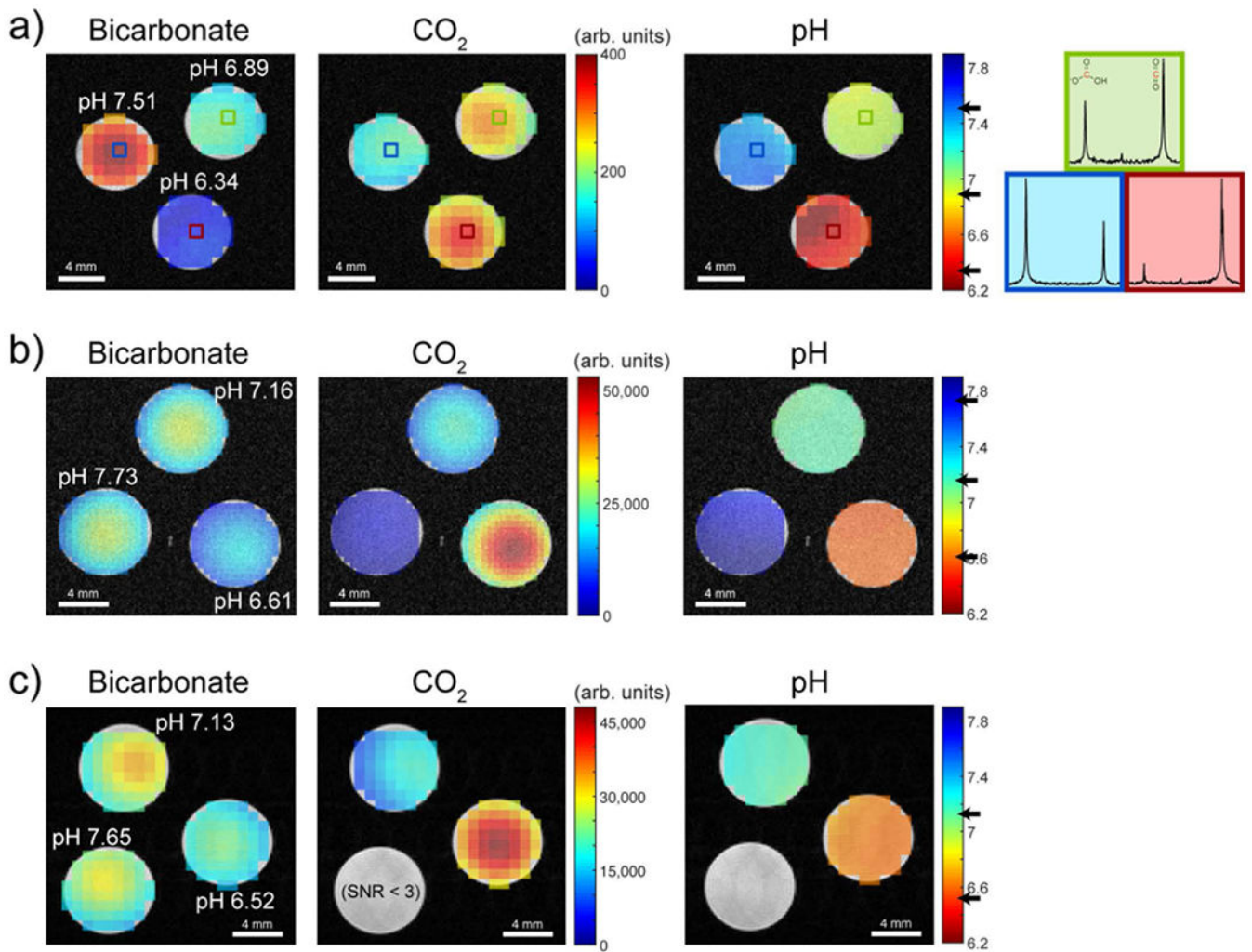7.6).

Figure 5:
Representative phantom images of three pulse sequences evaluated in this study, showing signal in each tube plus calculated pH maps. Each set of images was acquired during a separate HP experiment. (a) 2D CSI with $[2.78°,25°]$ BiC/CO_2 excitation scheme. Representative spectra corresponding to the outlined voxels are displayed at far right. (b) 2D EPI with $10°$ BiC -> $90°$ CO_2 excitation scheme. (c) 3D GRASE imaging with $10°$ BiC -> $90°$ CO_2 excitation and 2-band refocusing scheme. The electrode pH for each tube measured after HP imaging is indicated on the bicarbonate images. All imaging data were zero-filled 4x spatially and Gaussian filtered in-plane (12 dB signal attenuation at edges) for display purposes. 2D CSI data were 10 Hz apodized spectrally. Black arrows indicate the electrode-measured pH values on the pH color bar.
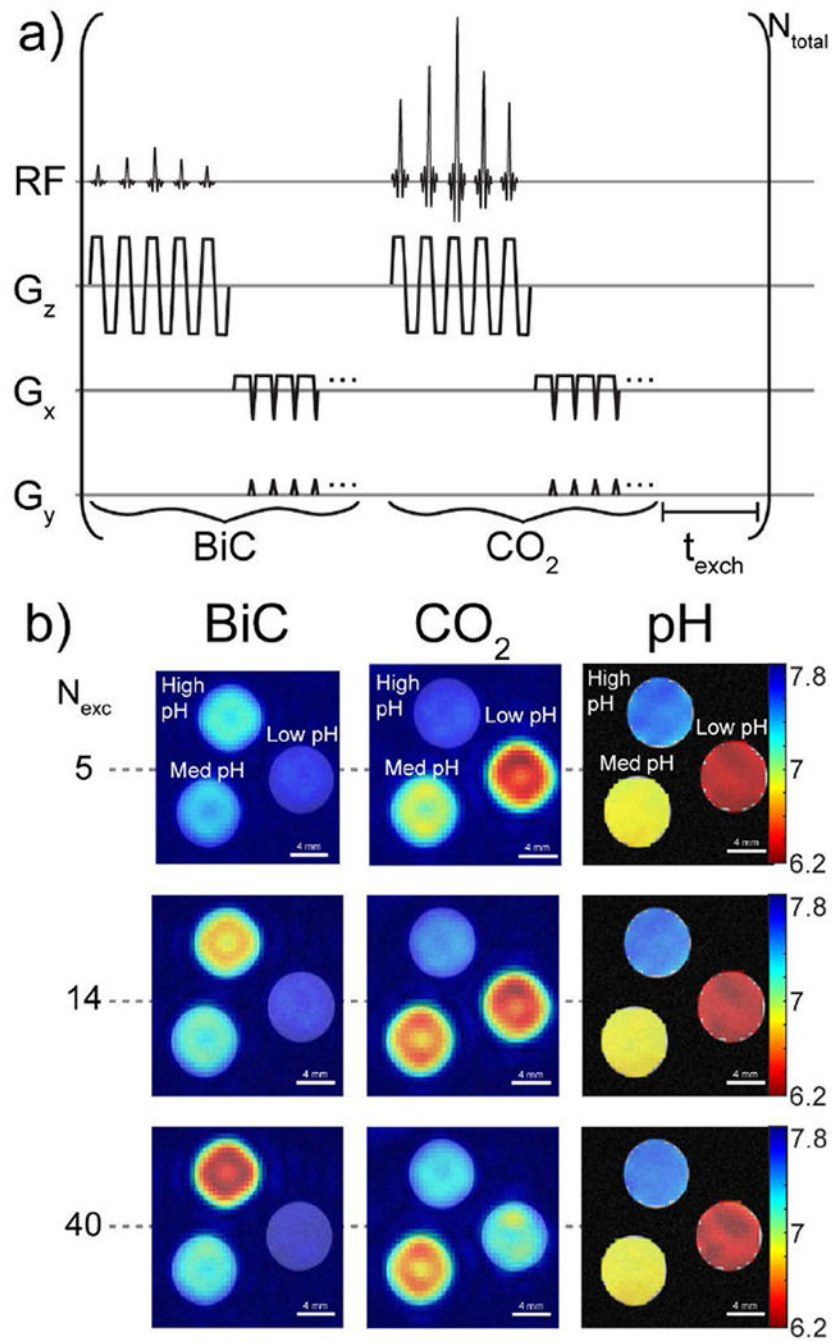
Figure 6:
Hyperpolarized pH imaging using a 2D EPI with multiple acquisitions (multi-EPI) approach. (a) Pulse sequence diagram for the pulse sequence. 2D EPI with spectral-spatial excitation is performed on BiC, then CO_2. A time delay t_{exch} is included in order to bring the imaging TR up to the value determined via simulation. The sequence is performed N_{total} times. (b) Bicarbonate and CO_2 maps obtained by summing acquisitions 1 to N_{exc} N_{total} to maximize CO_2 SNR for each pH value, along with corresponding pH maps, for a representative phantom experiment.
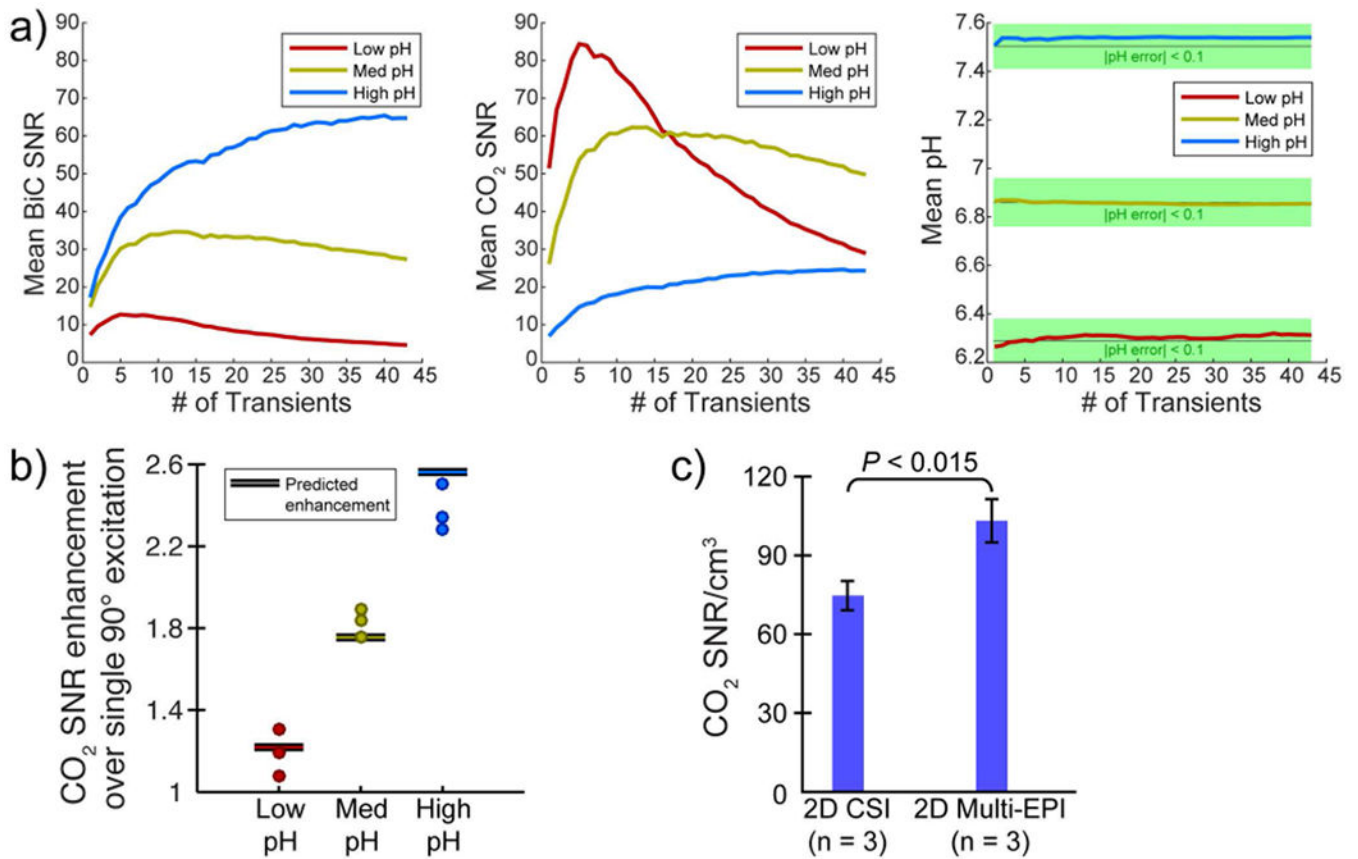
Figure 7:
Improved HP pH imaging SNR with 2D multi-EPI. (a) Plots of mean bicarbonate/CO_2 SNR and pH as a function of summed transients corresponding to the images in Figure 6b. The imaging pH remained within ± 0.1 unit of the electrode-measured value over all acquisitions. (b) Scatter plots of calculated CO_2 SNR enhancement over a single 90° acquisition per tube for n = 3 phantom experiments. The mean enhancement for each pH was within $\pm 10\%$ of the value predicted by simulation. (c) Volume-normalized CO_2 SNR comparison between 2D multi-EPI and 2D CSI [2.78°,25°] sequences (accounting for in-plane/slice profile broadening via simulation). The multi-EPI approach afforded a statistically significant mean SNR enhancement of 38%.

Table 1:

Details of pulse sequences used for phantom pH imaging.

Sequence	Excitation pulse	Matrix size	Nominal Resolution (mm³)	TR (ms)	Total imaging time (s)
2D CSI	2-band Gaussian (9) 1.9 ms length 1500 Hz bandwidth *Excitation schemes:* 1) 10° each 2) 2.78° BiC, 25° CO_2	8×8×256	4×4×10	67	4.3
2D EPI	Spectral-spatial (26) 6.7 ms length 300 Hz bandwidths *Excitation schemes:* 1) 90° CO_2 -> 90° BiC 2) 10° BiC -> 90° CO_2 3) 5° BiC -> 52° CO_2 (multi-EPI)	16×16	2.5×2.5×8	21 (multi-EPI: 330)	0.042 (multi-EPI: 14.2)
3D GRASE	Spectral SLR (22) 6 ms length 500 Hz bandwidth *Excitation scheme:* 10° BiC, then 90° CO_2	12×12×16	3.3×3.3×2.5	156	0.23

Table 2:

Literature summary of experimental results measuring first-order bicarbonate-CO_2 kinetic rate constants in various biological systems. All values correspond to a temperature of 37 °C unless otherwise noted. Values in italics are calculated from figures and/or numbers reported within literature sources.

Reference	(Biological) system	pH	k_{bc}	k_{cb}	$k_{ex} = k_{bc} + k_{cb}$
(40)	Solution, no CA catalysis	7	*0.02*	*0.15*	*0.17*
(29)	Solution, 8 µg/mL CAII added	7.4	0.25	*4.25*	*4.50*
This work	Solution, 7.6 µg/mL CAII added	6.7	1.34	4.17	5.51
(41)	*In vivo*, no CA catalysis	7.4	*0.01*	0.13	*0.14*
(42)	Lysed whole blood	7.4	*2.4*	43.2	*45.6*
	Whole blood (extrapolated from figure)	7.4	*0.08*	*1.39*	*1.47*
(43)	Guinea-pig ventricular myocyte cytoplasm, CA inhibited	7.6	*0.005*	0.144	*0.149*
	Guinea-pig ventricular myocyte cytoplasm, no CA inhibition	7.6	*0.01*	0.36	*0.37*
(4)	EL4 lymphoma cell xenograft, mouse	7.1	*0.79*	*6.74*	*7.53*
(29)	HCT116 colorectal cell xenograft, mouse	6.8	*0.16*	*0.82*	*0.98*
	HCT116 colorectal cell xenograft, mouse, CAIX overexpressed	6.7	*0.13*	*0.47*	*0.60*
This work	TRAMP mouse tumor	7.2	0.15	1.41	1.56

Table 3:

Summary of effects of rapid exchange (relative to imaging timescales) on spatial resolution, CO_2 signal-to-noise ratio, and pH accuracy. The 2D multi-EPI uses the same sequence as the 2D EPI but repeats it multiple times and sums timepoints together. Note that this table neglects effects of rapid BiC-CO_2 exchange in between separate BiC and CO_2 excitations for the 2D multi-EPI; these effects will follow the same trends as the regular 2D EPI.

			Effects of rapid BiC<->CO_2 exchange on …	
Sequence	In-plane resolution	Slice profile	CO_2 SNR	pH accuracy
2D CSI	BiC+CO_2 experience similar PSF broadening	BiC+CO_2 have similar slice profiles	Equal tip angles: No effect Higher tip on CO_2: CO_2 SNR boosted	Equal tip angles: No effect Unequal tip angles: Maintains pH accuracy
2D EPI	None	None	BiC excited first: CO_2 SNR decreases with increasing BiC tip CO_2 excited first: No effect	BiC excited first: pH overestimated CO_2 excited first: pH underestimated
2D Multi-EPI	None	BiC+CO_2 have similar slice profiles	Equal tip angles: No effect Higher tip on CO_2: CO_2 SNR boosted	Equal tip angles: No effect Unequal tip angles: Maintains pH accuracy
3D GRASE	None	None	1-band refocusing: Severe CO_2 signal loss (BiC excited first, small tip) 2-band refocusing: Same as 2D EPI, based upon which resonance excited first	1-band refocusing: Severe pH overestimation (BiC excited first, small tip) 2-band refocusing: Same as 2D EPI, based upon which resonance excited first